Tribological behaviour of 316L stainless steel additively manufactured by laser powder bed fusion and processed via high-pressure torsion

Shahir Mohd Yusuf[a], Daryl Lim [a], Ying Chen[b], Shoufeng Yang[a,c], and Nong Gao[a,*]

[a]Materials Research Group, Faculty of Engineering and Physical Sciences, University of Southampton, Southampton SO17 1BJ, UK

[b]Fujian Provincial Key Laboratory of Functional Materials and Applications, Xiamen University of Technology, Xiamen 361024, PR China

[c] Production Engineering, Machine Design and Automation Section, Department of Mechanical Engineering, Katholieke Universiteit Leuven (KU Leuven), Leuven 3001, Belgium

ABSTRACT

For the first time, the tribological behaviour of 316L stainless steel (316L SS) additively manufactured via laser powder bed fusion (L-PBF) with ultrafine- and nano-grains obtained from high-pressure torsion (HPT) processing has been investigated. The by pin-on-disk dry sliding wear test results demonstrate enhancement wear performance after HPT processing, as indicated by the consistently lower coefficient of friction (COF), mass loss, *m* and specific wear rate, *k* values than the as-received state. The improvement in overall wear resistance could be attributed to the significantly high hardness obtained due to the nano-scale grain refinement with increasing torsional strains. Microscopy analysis suggests that the wear mechanism transitioned from severe abrasive wear before HPT to a combination of mild abrasive, adhesive, and tribo-oxidative wear after HPT.

Keywords: Tribology; dry sliding wear; pin-on-disk; wear mechanisms; laser powder bed fusion; high-pressure torsion

* Corresponding author.

E-mail addresses: symy1g12@soton.ac.uk (S Mohd Yusuf), cydl1n15@soton.ac.uk (D. Lim), cyj829@163.com (Y. Chen), shoufeng.yang@kuleuven.be Shoufeng Yang (S. Yang), n.gao@soton.ac.uk (N. Gao).

1. Introduction

In laser powder bed fusion (L-PBF) metal additive manufacturing (AM) technology, successive metal powder bed layers are selectively melt and fused together by using a laser heat source to form a three-dimensional (3D) structure based on the input computer aided design (CAD) file. L-PBF AM techniques such as selective laser melting (SLM) has been used to fabricate various engineering applications, particularly in the aerospace, biomedical, and automotive industries. Compared to wrought, cast, and other conventionally manufactured (CM) metals, some of the advantages of AM include tremendous design flexibility, shorter lead times, and reduced waste of materials, as explained by Yusuf and Gao (2017) in their review of the energy density impact on the metallurgy-property relationship of AM metallic materials. In addition, Lewandowski and Seifi (2016) reviewed the properties of many AM alloys fabricated under various conditions, e.g. part orientation, post-processing methods and reported that AM metallic structures possess unique mechanical, wear, corrosion, and fatigue properties, either improved or comparable to their CM counterparts.

Differently, the application of large amounts of strains on bulk metallic materials via severe plastic deformation (SPD) techniques have been shown to produce materials with ultrafine-grained (UFG) and nano-grained (NG) microstructures, with enhanced mechanical properties, particularly the yield and tensile strengths, and superplasticity at room temperature, as explained by Azushima et al. (2008). From the various SPD techniques, equal channel angular pressing (ECAP) and high-pressure torsion (HPT) are the most widely used. In particular, HPT is considered the most efficient because of its simple operating mechanism and its capability of producing grain boundaries with high misorientation angles in large amounts, as explained by Wongsa-Ngam et al. (2013) whom compared the microstructures and properties of Cu-Zr obtained by using ECAP and HPT SPD techniques. Furthermore, Zhilyaev et al. (2003) confirmed the effectiveness of HPT to obtain bulk nanometer sized grains in their study of HPT-processed Ni.

316L SS is used in a wide range of applications, including marine engineering, facilities for storage and preparation of food and beverage (F & B), biomedical implants, and nuclear reactor parts as a result of the superior toughness and excellent corrosion resistance of this material. It is an austenitic steel, in which the high chromium content (up to 18%) contributes to the exceptional corrosion resistance, while the low carbon content (denoted by the letter ‘L’)

reduces the susceptibility to form carbides that may cause corrosion cracking. However, 316L SS and other low carbon SS cannot be strengthened by heat treatment procedures due to the inability to form strengthening precipitates as the result of the low carbon content. Therefore, the only way to strengthen 316L SS alloy is through work hardening, and SPD processes are well suited for this purpose because of the generation of numerous dislocations as well as UFG and NG microstructures. Gubicza et al. (2016) conducted HPT processing on wrought 316L SS and observed significant hardness increase after 10 revolutions (~610 HV) compared to the as-received condition (~155 HV). They explained that such high increment was the result of the ultrafine grain sizes and increased density of dislocations. Abramova et al. (2014) attributed the high strength of HPT-processed wrought 316 SS (~1700 MPa) to the ultrafine grain sizes, high dislocation densities grain boundary segregation, and twinning mechanism. Karavaeva et al. (2015) compared the strength of rolled, ECAP-processed, and ECAP+rolled wrought austenitic SS, and found that the ECAP+rolled specimens possess the highest ultimate tensile strength (UTS) value of 1720 MPa, >700 MPa of the ECAP-processed counterpart. The combined influence of grain boundary, dislocation, and twins were determined to be the strengthening mechanisms that resulted in such high UTS value. On the other hand, Chen et al. (2019) recently confirmed that the presence of nano-oxide silicate particles in SLM-fabricated 316L SS is able to increase its yield and tensile strengths by forming nano-precipitates after suitable post-processing heat treatments.

The importance of tribology in many modern engineering applications cannot be underestimated, particularly for those involving the rubbing or sliding of two materials against each other, e.g. biomedical implants and moving parts in F & B machineries. Therefore, tribological performance, or more specifically, wear resistance is a crucial criterion in the engineering design stage for applications of 316L SS. So far, tribological property studies on 316L SS additively manufactured by SLM has involved wear testing at both dry and lubricated conditions. Li et al. (2018a) investigated the impact of build direction, temperature, load, and frequency on the wear properties of 316L SS fabricated by SLM by utilising a ball-on-plate test rig. The following conclusions were made from their study: (i) build-up direction had no impact on wear resistance, (ii) coefficient of friction (COF) decreased at higher test temperatures, with the lowest wear rate obtained at room temperature, (iii) and higher wear rate was observed at higher loads although the COF was not influenced significantly. In another investigation, Li et al., (2018b) also found insignificant COF and wear rate differences in the of 316L SS manufactured by SLM when varying the laser power parameter.

Sun et al. (2014) researched the tribological behaviour of SLM-fabricated 316L SS at different scan speeds and found that samples with porosities ranging from 1.7 to 6.7% possess poor sliding wear resistances, thus suggesting improved wear performance in samples with high densification levels. Zhu et al. (2016) investigated the tribological properties of additively manufactured 316L SS by SLM under lubricated condition via ring-on-disk test configuration, and reported improved COF compared to CM 316L SS. Bartolomeu et al. (2017) compared the mechanical and wear behaviour of 316L SS manufactured by SLM with that of cast and hot-pressed counterparts, and they found that SLM 316L SS had the highest yield and tensile strengths and the best wear performance. In addition, Valentini et al. (2002) concluded that the higher hardness of SLM-fabricated 316L SS contributes to its improved wear resistance compared to that of its CM counterpart.

On the other hand, not many studies have investigated the tribological properties of SPD-processed bulk UFG/NG 316L SS. For example, Muley et al. (2016) assessed the corrosion and wear behaviour of UFG 316L SS obtained by multiaxial forging (MAF) for implant applications. They found that the improved sliding wear resistance was due to the change of abrasive wear mechanism from micro-cutting to wedge-formation as a result of high hardness and much finer grain sizes with increasing MAF strain levels. Nevertheless, there are indeed some studies on the wear performance of surface-nanostructured 316L SS obtained by other techniques. Sami and Mahdi (2018) studied the influence of nanostructured surface layer created by surface mechanical attrition treatment (SMAT) on the wear performance of CM 316L SS. It was found that the reduced COF and enhanced wear resistance of the nanocrystalline layer was the result of higher hardness, reduced grain sizes, and martensitic transformation at the SMAT-modified layer, in contrast with that of its coarse-grained (non-SMAT-modified) counterpart. Amanov et al. (2017) found remarkable enhancements in COF and wear resistance, together with high yield strength of a nanocrystalline layer on 316L SS obtained by ultrasonic nanocrystalline surface modification (UNSM) treatment, which were attributed to the increased hardness after the treatment. Rezaei-Nejad et al. (2015) studied the microstructural alteration on the surface of a 316L SS plate using friction stir processing (FSP). Remarkable reductions in COF and wear rate were attained, which were ascribed to the low plastic deformation level at the hardened FSP surface, leading to lower frictions and decreased adhesive and abrasive wear.

However, the influence of UFG and NG microstructures obtained by HPT processing on the wear performance of 316L SS additively manufactured by SLM has not been investigated yet. In the present study, SLM was used to additively manufacture 316L SS specimens, followed by HPT processing through 1/4, 1, and 10 revolutions. The wear performance was tested using a pin-on-disk test configuration via a dry sliding wear approach. The coefficient of friction (COF) and wear rate parameters were also calculated to quantitatively assess the wear resistance before and after HPT processing.

2. Materials and methods

2.1 Material and sample preparation

Table 1 lists the processing parameters and conditions applied for the Concept Laser M2 SLM machine used to additively manufacture a cylindrical rod of 316L SS material (length: 200 mm, diameter: 10 mm).

Table 1
Processing parameters and conditions applied for SLM fabrication of 316L SS in this study.

Parameter	Value
Laser power, *P*	200 W
Scan speed, *v*	1600 mm s^{-1}
Layer thickness	30 µm
Scan strategy	Island (checkerboard)

On the other hand, Table 2 displays the chemical composition of the 316L powder used in this study, which is similar to those used by Mohd Yusuf et al. (2020) in their study on the HPT processing of SLM-fabricated 316L SS.

Table 2
316L SS chemical composition used in this study (wt. %) based on Mohd Yusuf et al. (2020).

	Cr	Ni	Mo	Mn	Si	C	P	S	Fe
316L SS	16.5-18.5	10.0-13.0	2.0-2.5	0-2.0	0-1.0	0-0.030	0-0.045	0-0.030	*Bal.*

HPT samples were prepared by slicing the as-received rod into thin disks of 1 mm in thickness, followed by using of 800 grits of SiC abrasive paper for mechanical grinding down to ~0.85

mm. HPT processing was conducted by applying compressive force and torsional strain simultaneously using HPT facility described by Mohd Yusuf et al. (2018) in their initial work of HPT processing 316L SS additively manufactured by SLM. HPT experiments were conducted at room temperature (RT) under a constant 6 GPa pressure for 1/4, 1, and 10 revolutions that yield different amounts of torsional strain. The following equation is used to estimate the HPT-imposed von mises equivalent strain, $\varepsilon_{eq.}$ (Edalati and Horita, 2016):

$$\varepsilon_{eq} = \frac{2\pi NR}{h\sqrt{3}} \quad (1)$$

N: number of HPT revolutions, *R*: distance from the centre of the disk, and *h*: thickness of initial disk before HPT processing.

2.2 Microstructural characterisation

Microstructural characterisations were conducted using OM-Olympus BX-51 optical microscope (OM), JSM-JEOL 6500 field emission scanning electron microscope (SEM), and FEI TalosTMF200 transmission electron microscope (TEM). The OM, SEM, and TEM observations were carried out at the peripheral regions, 3 mm from the centre of the disks. Before observations through OM and SEM, the disks were mechanically ground using SiC abrasive papers (1200 and 4000 grits) and then polished using 3 and 1 µm diamond suspensions to attain mirror-like surface finish, followed by etching via Kalling's reagent (No. 2) to reveal the microstructures. In preparation for TEM, 3 mm small samples were punched out from the disks at a location of 3 mm from the centre. Thin films were then extracted from the 3 mm samples by using a Model 656 dimple grinder and Gatan-supplied precision ion polishing system (PIPS). The mean size of the grains were measured using the intercept method based on 20 micrographs for each processing condition, considering at least 100 grains from each micrograph, as described by Thorvaldsen (1997) whom evaluated the grain shape of polycrystalline materials by using this approach.

2.3 Wear testing and microhardness measurements

To assess the wear, dry sliding reciprocating wear tests were carried out on a TE 77 tribometer in a linear reciprocating pin-on-disk mode. The disks were secured on a mild steel plate using

adhesive, which was then fixed onto the lower clamp. The counter surface, i.e. the pin was an alumina ball (diameter: 6 mm, hardness: 1160 HV), fixed inside the top clamp, which will glide on the surface of the disks in a linear back and forth (reciprocating) manner during the wear tests. The complete setup of the wear test rig used in this study is illustrated by Wang et al. (2011) in their investigation of the wear properties of ECAP-processed Al alloy.

Prior to test, SiC papers (800 – 4000 grits) were used to ground the disks, which were then polished down to 3 μm and 1μm diamond suspensions. The disks were subsequently cleaned using isopropanol, dried, and weighed before being glued on to the mild steel plate. After each testing, the adhesive that secured the disks and mild steel plate were removed by using an ultrasonic acetone bath. The disks and mild steel plate were further cleaned in the same bath for 10 minutes to remove any debris or dirt on the surface. Finally, a Mettler AE240 microbalance (± 0.1 mg) was used to determine the mass loss due to material removal during the wear tests. In addition, the alumina ball is replaced for each disk due to slight wear and deformation on the ball after testing for ensuring consistency across all test conditions.

The dry sliding wear tests were carried out at the disk peripheries, ≥ 3 mm from the centre to be consistent with the location of microstructural observations. The load applied was 5 N, consistent throughout all processing conditions. The alumina ball (counter surface) glided with a 2 mm stroke length under 1 Hz reciprocating frequency, resulting in a 4 mm s^{-1} mean sliding velocity. The temperature and humidity during testing were 21°C and 30.3 %, respectively. A total of 8 separate tests were conducted at 8 different peripheral locations on the disk to obtain average values when determining the tribological properties, as described by Han et al. (2017) whom investigated the micro-mechanical and tribological behaviour of HPT-processed Al-Mg small disk samples (Fig. 1). Future Tech FM-300 machine was used to measure the Vickers microhardness (HV) values at each of these 8 locations under a load of 100 gf with a dwell time of 15 s. 20 individual indents were made at each location for a total of 160 indents and then averaged to obtain the microhardness value for each disk.

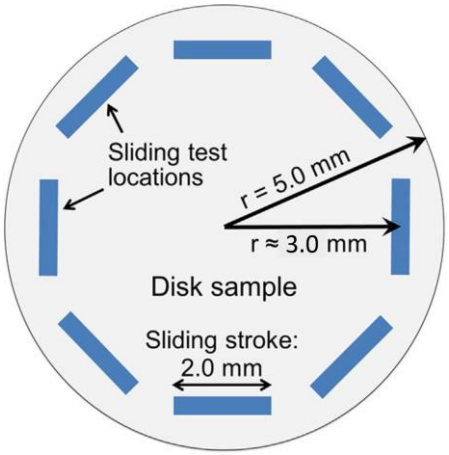

Fig. 1 Description of wear test location on the disk by Han et al. (2017).

The coefficient of friction (COF) was measured using COMPEND 2000 software attached to the wear rig setup for an overall 20 m sliding distance at each test location in all processing conditions. The surface roughness was measured using the Alicona infinite focus microscopy (IFM) system before and after wear tests, while 2D and 3D surface profiles of the surface roughness topology of the disks were created and analysed by using the TAICAAN XYRIS 2000 TL/CL metrology system. SEM and electron dispersive x-ray spectroscopy (EDX) analysis were conducted to assess the morphologies and microstructures of the worn surfaces.

3. Results

3.1 Evolution of microstructure and microhardness

Fig. 2 displays the microstructure for the as-received disks (Figs. 2(a) and (b)) and after 10 HPT revolutions (Figs. 2(c) and (d)). A combination of fine and coarse grains, averaging ~40 µm with some pores (black spots) can be observed from the deep-etched OM image in Fig. 2(a), while Fig. 2(b) displays the SEM image of columnar and equiaxed cellular sub-structures in the as-received disk. Furthermore, the TEM image of an equiaxed cell (inset of Fig. 2(b)) reveals the accumulation of dense dislocations within the cellular sub-structures. On the other hand, after 1/4 and 1 HPT revolution, the mean grain sizes are reduced to ~118 nm and ~68 nm, respectively. After 10 HPT revolutions, the SEM image in Fig. 2(c) reveals cellular network annihilation, with a final average grain size of ~42 nm is obtained at this saturation stage, as shown by the TEM image in Fig. 2(d). The detailed microstructural evolution for disks before and after HPT processing are described by the current authors in their previous studies of the microstructural evolution and strengthening (Mohd Yusuf et al., 2019), corrosion

performance (Mohd Yusuf et al., 2018), and micro-mechanical response (Mohd Yusuf et al., 2020) of 316L SS manufactured by SLM and then processed by HPT. In general, these observations are in agreement with various studies for many metals and alloys that reported a saturation in grain refinement is obtained upon higher number of HPT revolutions, e.g. after 10 revolutions, which could be caused by the combination of: (i) dislocation accumulation and grain refinement that causes hardening, and (ii) dislocation annihilation and grain recrystallisation that results in softening. Scheriau et al. (2011) also observed a similar mutual hardening and softening phenomenon when processing a modified 316L SS by HPT at room temperature. They explained that the steady state ultrafine and nano-scale grain sizes obtained at saturation stage are caused by the balance of production and elimination of dislocations due to the plastic shearing induced during HPT processing.

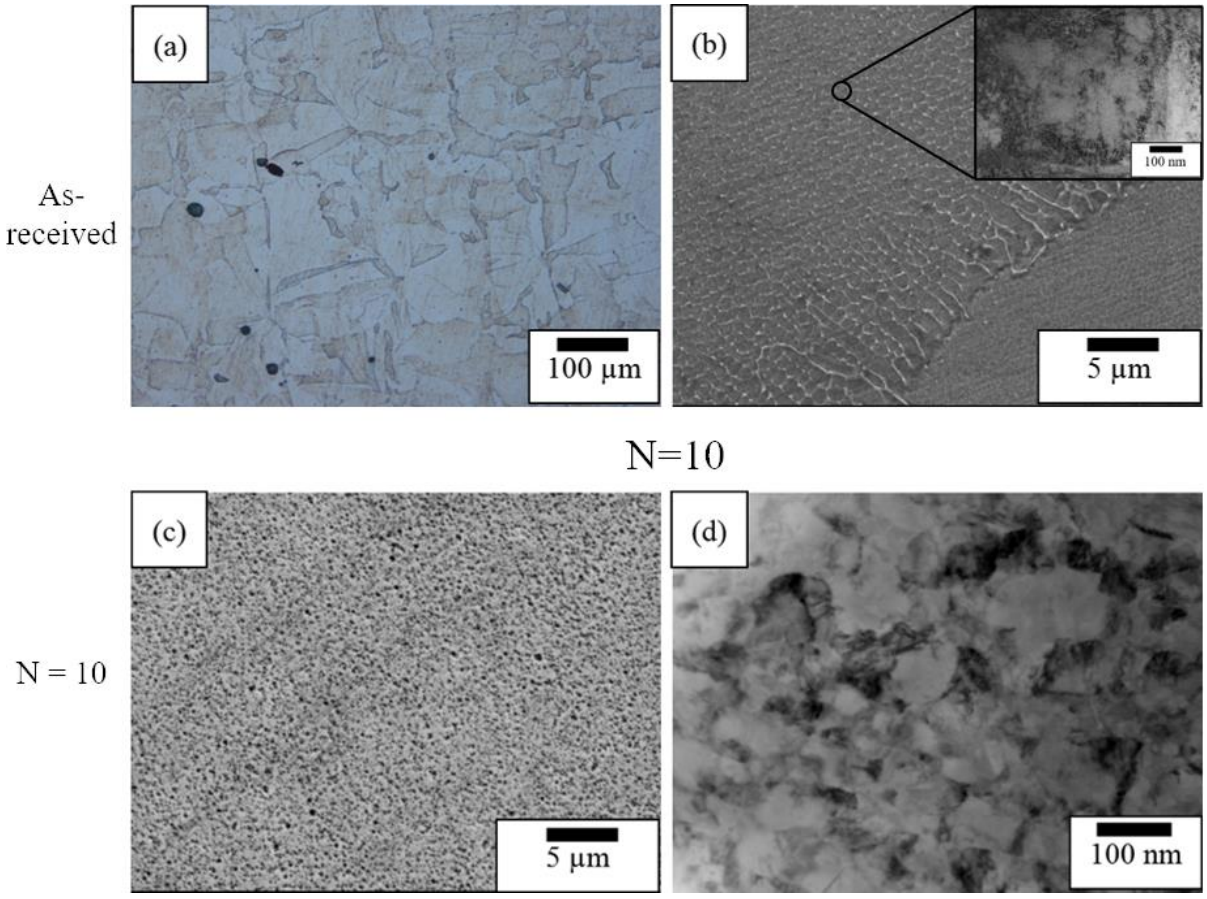

Fig. 2 Representative microstructures before HPT processing from (a) OM and (b) SEM (with TEM image of an equiaxed cell inset); and microstructures after 10 HPT revolutions from (c) SEM and (d) TEM.

Fig. 3 shows the evolution in HV values before (N = 0) and after (N = 1/4, 1, and 10) HPT processing at eight peripheral locations (3 mm from centre) corresponding to the wear test area as described in Fig. 1, with the associated error bars. The initial hardness before HPT

processing is measured as ~220 HV, which increases significantly to ~550 HV after only 1/4 revolution. The remarkable hardening at this early stage of HPT processing is attributed to both grain refinement and strong strain hardening effect as the result of considerable increase in the amount of dislocations. After 1 revolution, the hardness only slightly increases to ~590 HV before reaching a plateau at ~600 HV after 10 revolutions. At these later stages, the dislocations are not generated as much as during the initial HPT straining, thus the hardening is now mainly ascribed to the extreme grain refinements. The trend of hardness variation in this study is in agreement with many research on HPT-processed materials, which reported continuous increment in hardness at higher equivalent strain values during the initial HPT straining stage, and then saturates to a relatively constant value above certain strain values. These are usual characteristics of HPT-processed metals and alloys that display strong strain hardening without recovery at increasing equivalent strain values, as explained by Kawasaki et al. (2014) in their review of the evolution of hardness in various metals and alloys processed by HPT.

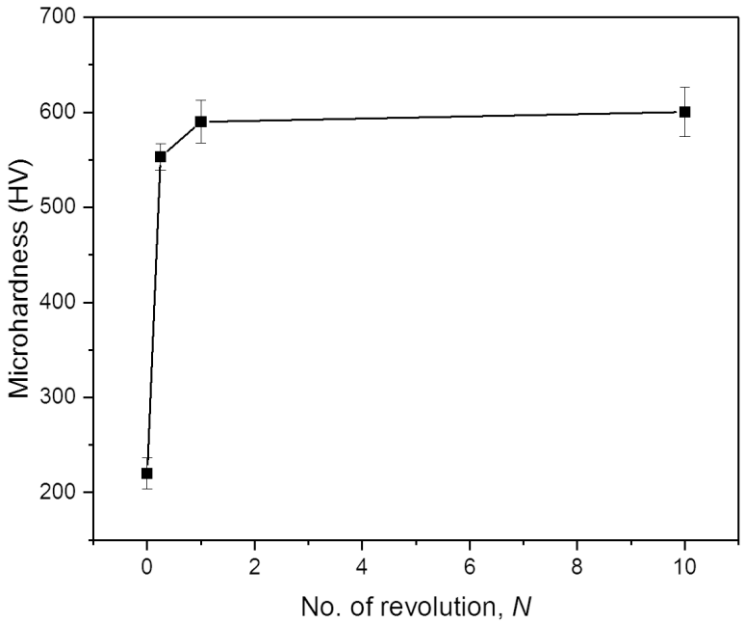

Fig. 3 Average HV values taken at 8 different locations 3 mm from the centre of the disks before and after HPT processing.

3.2 Wear properties

Fig. 4 displays the average COF and *m* values against *N* after wear testing at the given test conditions detailed previously. The wear test in this study was conducted with a reciprocating frequency of 1 Hz and continued for ~2000 s, thus the COF was recorded for a total of 2000 test points at 1 point per second. It is clear that HPT processing influences the measured COF values under the loading condition, with a continuous decrease from ~0.58 for the as-received

disk to ~0.43 after 10 revolutions, representing a ~26% reduction. Similarly, a 57% reduction in the mass loss was also observed with increasing HPT revolutions, from 26 ± 1 mg for the as-received condition to 11 ± 2 mg after 10 revolutions. It is reasonable to anticipate a reduced mass loss due to the higher hardness attained after HPT processing compared to the initial hardness before HPT processing, which is in line with Archard's equation proposed by Archard (1953) in his theoretical and experimental work on various aspects of wear for different materials. Here, he explained that the volume removed from the disks after wear testing, V (mass × density) is proportional to the inverse of material hardness, H, i.e. $V \propto 1/H$.

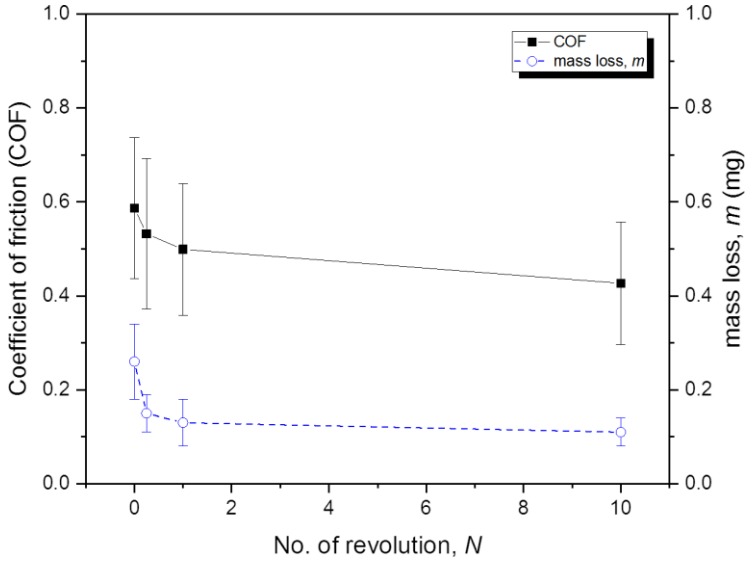

Fig. 4 Evolution of COF and *m* values before and after HPT processing.

Repeated contact between the alumina ball and the disk surface generates wear tracks, which are then used to generate wear scar profiles as shown in Fig. 5. These colour-coded two-dimensional (2D) visualisations were generated using the TAICAAN XYRIS 2000 TL/CL metrology system to illustrate and compare the depth along the wear scar across all disk conditions. The wear scar topographies shown in Fig. 5 indicate that the wear scar in the as-received disk is much deeper than that of the HPT-processed disks and it steadily decreases at higher HPT revolutions. In addition, Figs. 5(b) – (d) also show that the wear scar depth decreases across the boundary of the wear track to its centre with increasing number of HPT revolutions, as represented by the colour change from purple (deepest) to red (shallowest). It should be noted that the scale of the colour bars representing the wear track depth before and HPT processing is different; from -12 – 12 µm and from -6 – 2 µm, respectively. Such difference in wear depth could be attributed to the change in hardness. Since the material is comparatively softer before HPT processing, i.e. more ductile, the gliding movement of the counter surface (alumina ball) can easily deform the disk surface, thus allowing it to be

penetrated deeper into the material. On the other hand, the HPT-processed disks are harder, thus they are more difficult to be penetrated by the alumina ball. Therefore, only a small area of the surface could be deformed and some of the pressed surface are pushed towards the sides of the wear scar. As the hardness increases with the number of HPT revolutions, more pressed surfaces are pushed sideways, resulting in the higher surfaces at the edges and much shallower wear scar depth (Figs. 5(b)-(d)). These findings are similar to the shallower wear track depth observed on nano-grained surface layers of 316L SS obtained by various surface modification techniques. For example, Amanov et al. (2017) found that the substantial improvement in COF and tribological properties of UNSM-treated 316L SS tubing can be ascribed to the significant hardness increase in comparison with the non-treated counterpart. Rezaei-Nejad et al. (2015) used FSP to produce nanograins with sizes of 50 – 200 nm on the surface of 316L SS plates, and found that such remarkable grain refinement (from initial grain sizes of 30 – 40 μm) improved both the wear resistance and surface hardness by two- and three-fold, respectively. Sami and Mahdi (2018) showed that the creation of a nanostructured surface layer on SMAT-processed 316L SS significantly enhanced the corrosion and wear performance of the material.

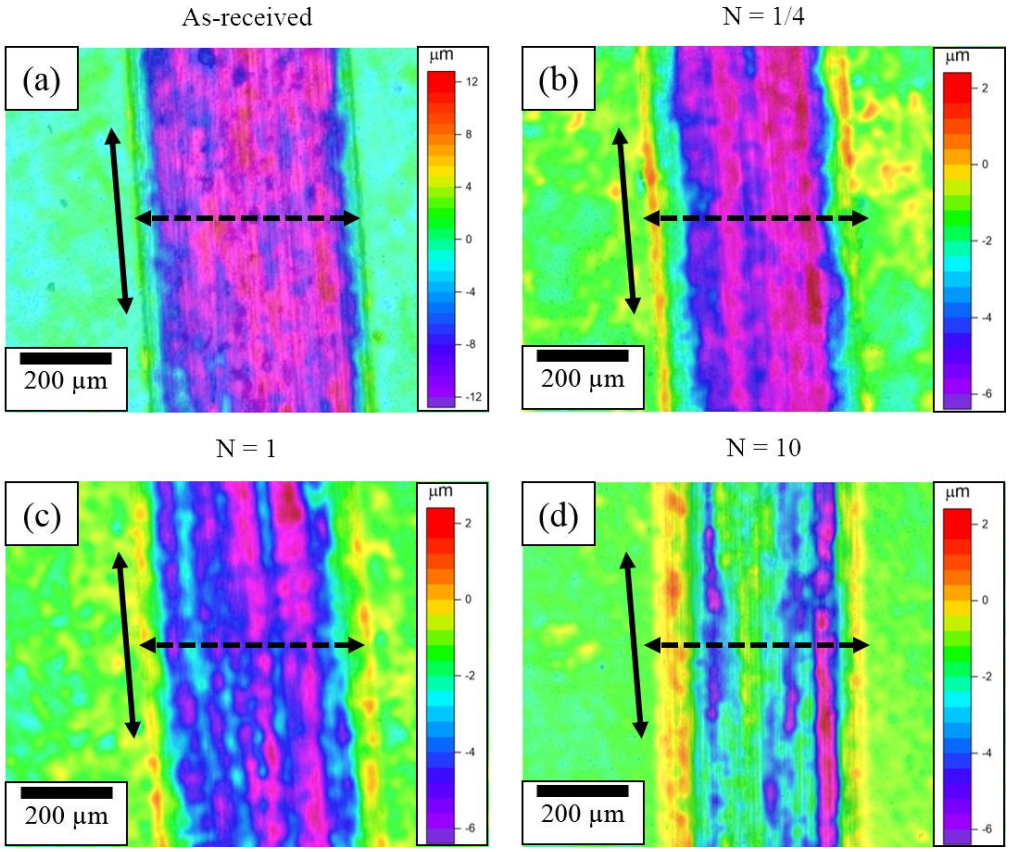

Fig. 5 2D analysis visualising the overall wear track depth of (a) as-received and (b) – (d) HPT-processed disks after wear test. Solid line shows sliding direction, dashed line show wear track width.

Fig. 6 demonstrates the averaged depth profile of the cross-sectional wear scar, taken from five randomly chosen lines along the wear scar for each disk condition and then evaluated using the Alicona IFM system. The dashed line across the 0 µm represents the boundary between wear grooves (inward curves towards more negative values) and wear ridges (outward curves towards more positive values). In general, a similar trend as Fig. 5 is observed; the wear scar depths (grooves) become progressively shallower with increasing HPT revolutions relative to that before HPT processing. Within the HPT-processed disks, the groove after 1 revolution is much shallower compared to that after 1/4 revolution, but only decreases slightly after 10 revolutions. In addition, some ridges are also formed at the wear track extremities, with the as-received disk having the largest amount compared to the HPT-processed disks as indicated by the highest peak and coverage area of the curve above the dashed line. The formation of ridges indicates material pile-up along the wear scar boundaries due to plastic deformation as the alumina ball slides along the wear track, commonly known as ploughing, coined by Kayaba et al. (1986) upon studying the wear performance of brass and steels under dry and lubricated conditions. However, the ploughing effect is less pronounced after HPT processing in contrast with the as-received disk, as indicated by the lower ridge peaks. These observations could be correlated to the fact that the hardness of the disk after saturation (10 revolutions) is close to that after 1 revolution, thus it becomes increasingly difficult to deform the disks. This is a common observation for most HPT-processed materials, in which HV values rapidly increase with increasing torsional strains at the early stages of HPT processing, but saturates to roughly constant values after achieving a certain equivalent strain value, as explained by Kato et al. (2015) in their study of the sliding wear behaviour of HPT-processed pure iron.

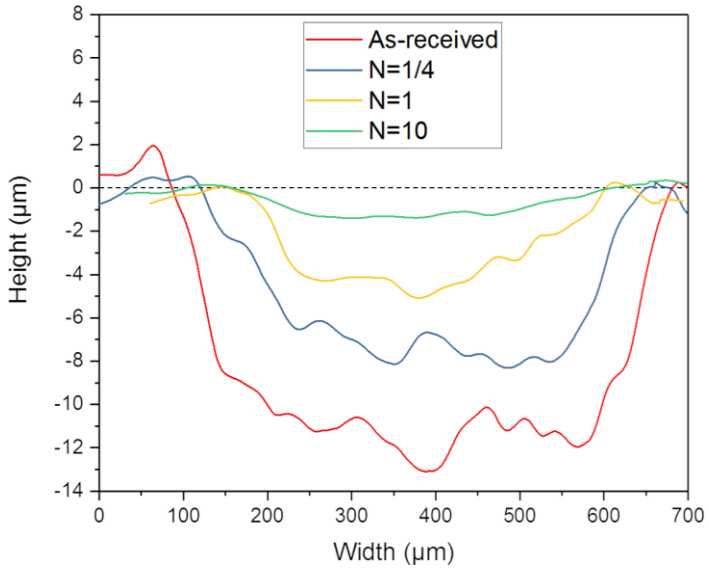

Fig. 6 Averaged wear depth taken from five different locations along the wear track measured by the surface profilometer. Dashed line indicates the original disk surface plane.

3.3 Worn surface morphologies

To further understand the tribological behaviour and characteristics before and after HPT processing, SEM observations and EDX analysis were carried out after the wear test. Fig. 7 exhibit SEM images of the evolution of surface morphology of the worn track for the as-received and HPT-processed disks, in which the double-arrow line indicates the sliding direction. The images consist of individual wear tracks taken at the centre and edge that are stitched together carefully to form a single continuous image for each disks condition. All disks exhibit straight grooves parallel to the sliding direction, indicating abrasive wear for all processing conditions. The sliding grooves displayed in Fig. 7 is consistent with the characteristics of abrasive wear in various metals described by Kato (1997) in their review of the principles and mechanisms of abrasive wear, which was explained in terms of plastic deformation work and fracture. The abrasive grooves appear deep, rough, and are closely spaced for the as-received disk (Fig. 7(a)). However, as the hardness increase with increasing HPT straining, the sliding grooves becomes progressively shallower, smoother, and more widely spaced (Figs. 7(b) – (d)) and the average COF values also gradually decrease (Fig. 4).

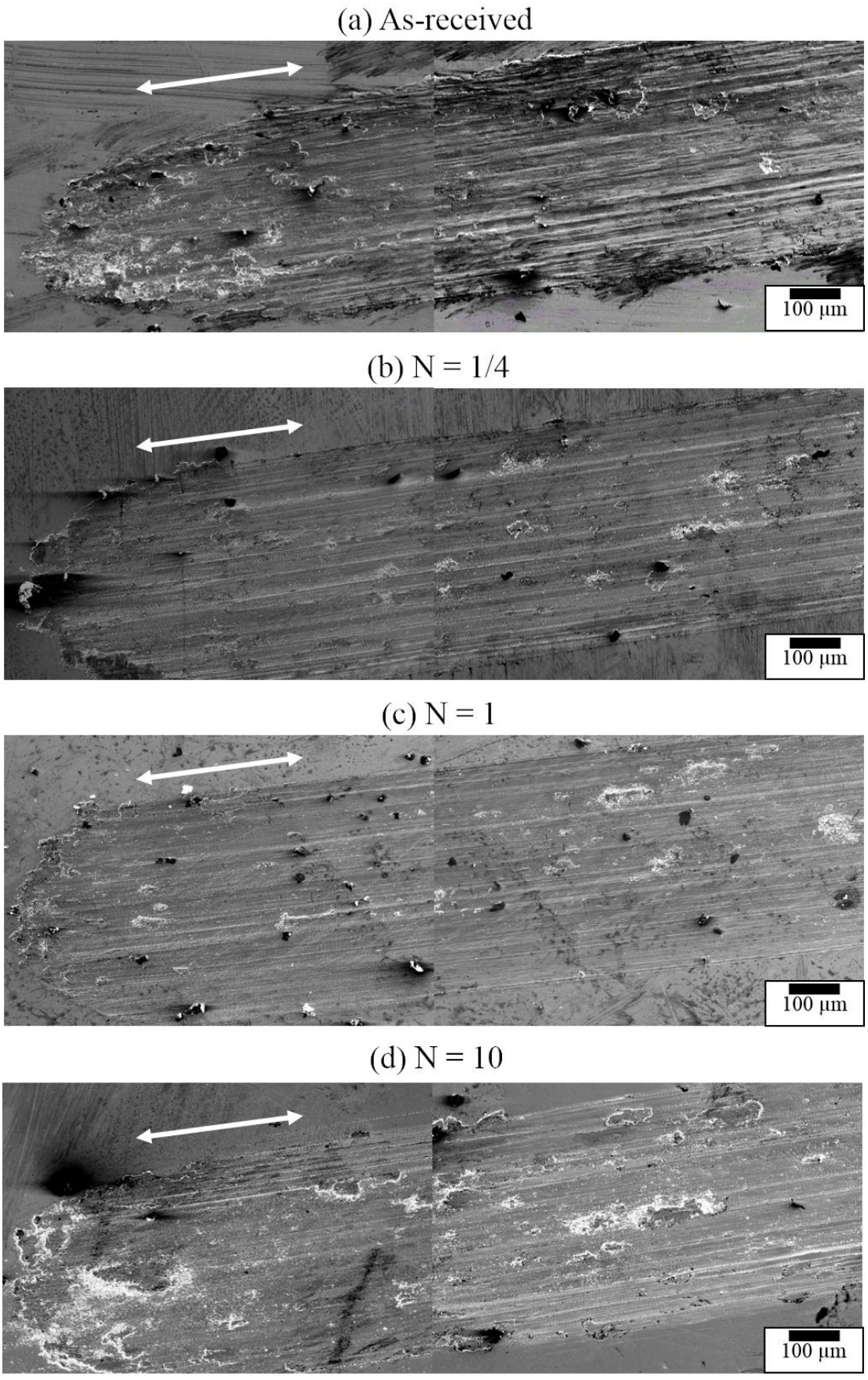

Fig. 7 SEM images of worn track surface for as-received and HPT-processed disks after wear test. Double-arrowed lines indicate sliding direction.

Furthermore, it is apparent that the characteristics of abrasive wear differ before and after HPT processing based on the disk surface morphology shown in Fig. 7. As can be observed for the as-received disk (Fig. 7(a)), some materials are pushed sideways from the centre of the wear track to form ridges along the sides of the groove. This confirms the occurrence of ploughing as shown in Fig. 5. However, ploughing does not occur in the HPT-processed disks. Instead, the harder counter surface (alumina ball) now removes and pushes some material on the relatively harder 316L SS surface from the centre towards the end of the wear tracks, which increase with the number of HPT revolutions (Figs. 7(b)-(d)). This phenomenon is called wedge formation or shear-tongue formation, another mode of abrasive wear (Kato, 1992).

In addition, Figs. 7(b) – (d) also shows that some of the areas within the wear tracks of HPT-processed disks are partly covered by irregularly shaped adhered wear particles as indicated by the bumpy surfaces, and their surface areas increase with higher torsional strains from 1 to 10 HPT revolutions. These adhered particles could be introduced via wear debris adhesion, or the back transfer of 316L SS (which was initially removed from the disk and attached to the alumina ball) from the surface of the alumina ball to the wear track surface, or even the material transfer of some alumina particles that are removed from the counter surface due to friction and then attached on the disk surface. This is similar to the findings by Bartolomeu et al. (2017) whom investigated the mechanical and wear performance of SLM-fabricated and conventionally manufactured 316L SS, in which the wear tests were conducted against an alumina ball under a sliding mode inside Phosphate Buffered Saline (PBS) fluid. Contrastingly, adhesive wear is less pronounced for the as-received disk in this study because it is relatively soft and the alumina ball can penetrate deep beyond its surface, resulting in minimal material removal. In addition, spherical (or close to spherical) black particles that seem to be wear debris could also be seen to be more apparent on the disk surface after HPT processing.

Fig. 8 displays higher magnification SEM images of the wear features on the surface of the disks before and after HPT processing. Fig. 8(a), taken at the wear track end of the as-received disk, exhibits solid arrows that show tear-like cuts perpendicular to the sliding grooves. These tears indicate micro-cutting, another mode of abrasive wear, which involves the removal of small chips from the softer material (316L SS) surface upon contact with the sliding counter surface (alumina ball), as explained by Muley et al. (2016) in their investigation on the corrosion and wear performance of wrought ultrafine grained 316L SS obtained through MAF technique for the purpose of implant applications. On the other hand, adhered wear particles

are apparent on the surface of the disks after 1/4 and 1 HPT revolutions as shown by the dashed arrows in Figs. 8(b) and (c), representing adhesive wear mechanism.

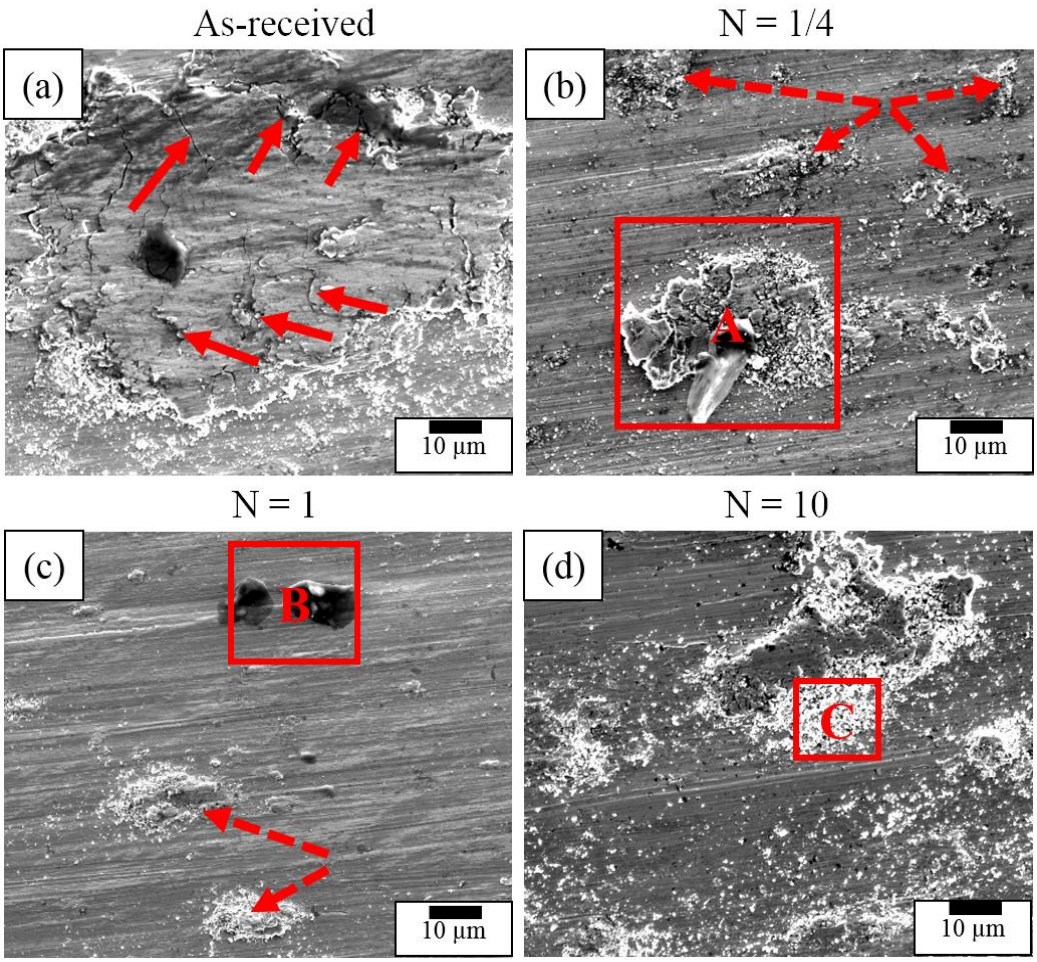

Fig. 8 Some wear features on the disk surface after wear test. Solid arrow shows micro-cutting, dashed arrows show material adhesion, and areas A, B, and C were subjected to EDX analysis.

To evaluate the characteristics of the wear features shown in Fig. 8 in more detail, EDX analysis was carried out on the three marked areas A, B, and C. Table 3 shows the resulting elemental composition of each area.

Table 3
The composition of elements in the wear features identified as A, B, and C in Fig. 8 (wt %).

Area	Fe	Cr	Ni	Al	O
A	77.25	4.16	2.04	-	16.55
B	-	-	-	83.34	16.66
C	72.11	2.59	-	-	25.33

It is revealed that the adhered wear particles (areas A and C) contain relatively large amounts of iron and oxygen and much less chromium and nickel, implying the occurrence of a mild tribo-oxidative wear. This is a common phenomenon in tribology tests on 316L SS, in which the protective chromium-based oxide layer is constantly removed by the repetitive rubbing of the counter surface on the base material. Hence, the bare 316L SS surface is exposed to air and can be easily oxidised to form an iron-based passive layer that is susceptible to rust and corrosion instead of the protective chromium-based oxide layer, as suggested by Li et al. (2018a) in their study of the tribological performance of SLM-fabricated 316L SS tested against E-52100 hardened steel in unlubricated condition. In addition, Kato (2008) investigated the influence of oxide particles on two rubbing steel surfaces, and explained that oxidation typically occurs in steel alloys and has been found to reduce the friction between the test material and the counter surface via compaction of fine oxidised wear particles that often results in smooth wear tracks and lower wear rates.

The COF values and EDX analysis clearly demonstrate that this is the case in the present study, suggesting that HPT processing is able to enhance the wear performance of 316L SS additively manufactured by SLM. In particular, white and bright areas or spots can be observed surrounding the adhered wear particles, which indicate a combination of adhesive and mild tribo-oxidative wear mechanisms after HPT processing, in addition to abrasive wear. Interestingly, the black particles that are initially thought to be just wear debris actually consists of aluminium and oxygen as shown by the EDX analysis for area B in Table 2, which is similar to the results of sliding wear test study on ECAP-processed commercially pure Al reported by Wang et al. (2011). Therefore, it is suggested that the black particles that are present on the surface of HPT-processed disks are aluminium-based oxide, i.e. alumina. They most likely detach from the alumina ball (counter surface) due to slightly increased friction upon sliding with the 316L SS surface as a result of increased hardness with increasing number of HPT revolutions, providing further evidence of adhesive wear. Therefore, it can be inferred from the current investigation that the wear mechanism transitions from severe abrasive wear for the as-received disk to a combination of mild abrasive, adhesive, and tribo-oxidative wear for the HPT-processed disks.

In addition, an example of a representative surface of alumina ball (counter surface) after dry sliding wear tests is shown by the SEM image in Fig. 9. Some wear particles are observed to be attached to the surface of the alumina ball, which could be 316L SS material removed from

the disk surface due to the repeated sliding between both materials. EDX analysis reveal the following chemical compositions (in wt. %); Fe: 35.9, Cr: 12.33, Ni: 8.46, Al: 19.07, and O: 24.24. Thus, the adhered wear particles on the alumina ball surface are indeed 316L SS material removed from the disk and then transferred to the alumina ball since the hardness of alumina is considerably higher than that of 316L SS.

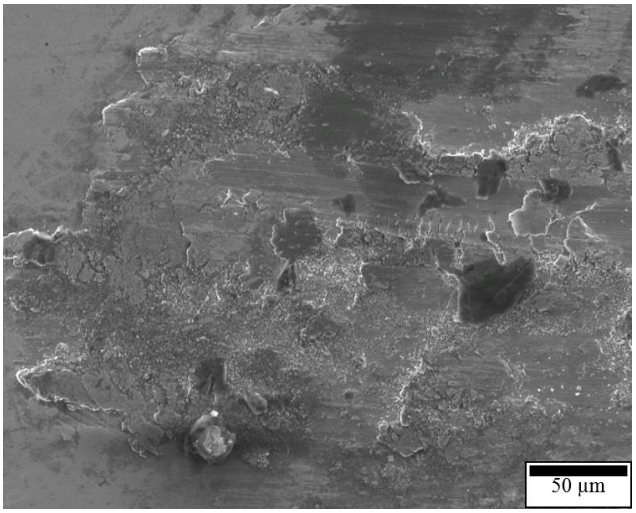

Fig. 9 SEM image of alumina ball surface after wear tests.

4. Discussion

In this study, HPT processing has been successfully applied to produce extreme grain refinement in SLM-fabricated 316L SS. Strain saturation is reached after 10 HPT revolutions with an average grain size of ~42 nm, significantly smaller than ~40 µm for the as-received disk. In addition, the hardness value also considerably increases from ~220 HV initially, to ~600 HV after 10 HPT revolutions. This maximum hardness value obtained at the saturation stage is comparable to that attained by Gubicza et al. (2016), ~610 HV after 10 HPT revolutions of wrought 316L SS, although saturation was not achieved in that study. This suggests similar response of HPT processing for both AM and wrought 316L SS in terms of significantly improving hardness and strength.

The results of the dry sliding wear tests in the current investigation provide valuable insight to the wear characteristics of UFG and NG SLM-fabricated 316L SS obtained through HPT processing. In addition to remarkable hardness increase, HPT processing also results in steady decrease in COF and *m* values with higher torsional strain levels as the number of HPT revolutions increase in comparison with the as-received condition (Fig. 4). Such low COF values attained after HPT processing can be explained in terms of the larger yield stress

required to produce plastic deformation as the hardness increases due to the extreme sub-micron/nano-scale grain refinement, thus increasing the resistance to sliding and reduces the friction between the base material (316L SS) and the counter surface (alumina ball). This finding echoes that of the study by Amanov et al. (2017) whom modified the surface of 316L SS tubing to be used as coronary artery stents by means of the UNSM technique. They found that the reduced friction coefficient resulting from the creation of UFG and NG microstructures on the surface of the material increased its yield strength, thereby requiring higher energy to be plastically deformed, which eventually increases sliding resistance.

Such reduction in COF due to refined grain sizes has also been observed in various studies on both surface and bulk nanostructuring of 316L SS and other SS alloys. For example, Roland et al. (2006) and Sami and Mahdi (2018) attributed the lower friction coefficient in SMAT-processed 316L SS layer in contrast with its untreated counterpart to nanostructured grains that were attained on the surface layer via SMAT. Rezaei-Nejad et al. (2015) studied the nanostructure layer formation on a 316L SS plate after FSP treatment. The grain sizes were observed to decrease from 30 μm to 50 – 200 nm, accompanied by significant hardness increase and enhancement in wear resistance. It was explained that the increased hardness of the FSP-treated layer was able to improve the coefficient of friction by limiting plastic deformation compared to the untreated regions for the same loading conditions of the wear test. Qin et al. (2018) compared the tribological behaviour in a dry air condition of a wrought 316L SS and a heterogeneous lamella-structured (HLS) 316L SS obtained by cold rolling and annealing. The HLS 316L SS possessed a mix of numerous lamella grains, nanograins, and nanotwins that increase the grain boundaries throughout the material bulk. It was found that the reduced friction and therefore, the COF value of HLS 316L SS compared to its wrought counterpart may be ascribed to the hard oxidative particles formed upon sliding at the interface during wear test as the result of these microstructural features.

Similarly, the reduced mass loss in HPT-processed disks in contrast to that before HPT processing in the current investigation is consistent with the conventional Archard's relationship that correlates mass loss with hardness given by Archard (1953):

$$V = k\frac{SL}{3H} \tag{2}$$

where V: loss of wear volume after wear test, k: material-specific dimensionless wear coefficient, S: sliding distance, L: load force imparted by the counter surface to the base material, and H: material hardness. This equation uses volume loss as an indicator of wear performance and suggests improved wear resistance i.e. reduced volume loss with increase in the hardness of the HPT-processed disks. Kato et al. (2015) conducted HPT processing on pure iron and also found out that the increase in hardness with HPT revolutions correspond to reduced volume loss and improved wear rates, thus confirming Archard's relationship between wear volume and hardness to assess the wear performance of HPT-processed materials.

The wear scar profiles evaluated using the surface profilometers (Figs. 5 and 6) indicate much deeper wear scars on the surface of the as-received disks compared to that on the HPT-processed disks and it steadily decreases with increased HPT revolutions. In addition, the wear scar morphologies observed through SEM (Fig. 7) show that all the as-received and HPT-processed disks experience abrasive wear. This occurs upon sliding due to either: (i) asperities or particles of harder materials (alumina ball in this study) on softer materials (316L SS in this study), or (ii) two similar materials that may cause the formation of hard particles. The occurrence of abrasive wear essentially removes some material from the surface of the softer 316L SS due to the repetitive sliding of the alumina ball on the disk surface.

It could be observed that the sliding grooves obtained for the as-received disk shown in Fig. 7(a) is very deep, rough and closely spaced between each other due to severe abrasive wear, which is related to the higher level of penetration into the as-received disk due to hard asperities, as explained by Hokkirigawa and Kato (1988) in their investigation of the formation of various abrasive wear mechanisms. In addition, the deeper grooves correspond to larger contact and impact between the base material and the counter surface, resulting in higher COF values, as described by Hutchings (1992) in their book regarding the friction and wear of engineering materials. Therefore, the increasingly shallower, smoother and more widely spaced grooves observed on the disks with higher HPT torsional straining compared to the as-received counterpart shown in Figs. 7(b) – (d) imply lesser contact and impact between both 316L SS and alumina ball surfaces since it becomes harder to deform the HPT-processed disks. This could explain the reduced COF values displayed in Fig. 4 and indicate that the initially severe abrasive wear mechanism for the as-received disk become gradually weaker after HPT processing at higher number of revolutions.

Furthermore, Figs. 7(b) – (d) also show evidence of mild adhesive wear mechanism that could be the result of adhered wear debris or the back transfer of 316L SS from the alumina ball surface to the wear track surface. This is similar to the findings in the study of sliding wear behaviour of pure iron processed by HPT, tested against WC-Co ball (counter surface) by Kato et al. (2015). They observed adhered wear particles on the surface of the test material (pure iron), which was confirmed to be adhered wear debris and back transfer of the test material from the counter surface. In 316L SS subjected to sliding wear tests, adhesive wear occurs due to the rubbing of the counter surface on the base material that eventually breaks down the protective oxide layer due to contact stress and results in a direct interfacial contact between both surfaces. Triwiyanto et al. (2013) observed a similar phenomenon in their study of the microstructures and wear characteristics of nitrided 316L SS. In the current investigation, it is possible that the formation of adhered wear particles is related to back transfer of 316L SS and material transfer of alumina particles from the counter surface. This is because, as the material progressively becomes harder with increased HPT torsional strain, it is more difficult to penetrate deep into the material, thus only the oxide layer and a few additional layers could be removed by the repetitive sliding. Thus, most of the surface of the material remain intact, and the removed 316L SS material could be attached to the alumina ball, before being transferred back and welded onto the surface of the disk. Similarly, the friction between the harder HPT-processed disks and the alumina ball could remove some alumina particles, which are then attached to the surface of the disks.

Therefore, the evolution of wear surface profiles, together with the results of COF and mass loss from the wear test in this study shown in Fig. 4 provide strong indications of progressive improvement of wear performance with increased HPT revolutions in comparison with the as-received disk. To confirm this inference and quantitatively evaluate the wear performance, the specific wear rate, *k*, i.e. the dimensionless wear coefficient derived from Eqn. 2 is used to estimate and directly compare the wear properties across all disk conditions given by Han et al. (2017):

$$k = \frac{V}{SL} \tag{3}$$

where *V*, *S*, and *L* are defined as in Eqn. 2. The volume loss, *V* is estimated by multiplying the area loss, *A* with stroke length, *l*. The area loss is estimated by analysing the wear scar profiles

using the TAICAAN XYRIS 2000 TL/CL surface profilometer to include both ridges and grooves of the wear tracks. The results of the calculated volume loss and the corresponding specific wear rate by applying Eqn. 3 for a constant 5 N load and 2 mm stroke length, and 20 m overall sliding distance are displayed in Table 4.

Table 4
Calculated *A*, *V*, and *k* values for the samples in the present study.

Sample	Area loss, *A* (mm^2)	Volume loss, *V* (mm^3)	Specific wear rate, *k* ($x\ 10^{-3}\ mm^3/Nm$)
As received	0.01625	0.0325	0.33
N = 1/4	0.00924	0.0185	0.19
N = 1	0.00798	0.0159	0.16
N = 10	0.00624	0.0125	0.13

The calculated *k* values confirm that the wear resistance of SLM-fabricated 316L SS is indeed enhanced by HPT processing, with reduction from 0.33×10^{-3} mm^3/Nm for the as-received disk to 0.19×10^{-3} mm^3/Nm after 1/4 revolutions (~42% reduction) and further decreases to 0.13×10^{-3} mm^3/Nm after 10 revolutions. This result is consistent with the Archard's relationship that suggests improvement in wear resistance with increased hardness of a material in general.

In addition, the influence of grain refinement down to the UFG and/or NG regime on the strength and wear performance of the studied material is also exemplified in Fig. 10, showing the microhardness, HV and specific wear rate, *k* evolutions as functions of inverse square root of grain sizes, $d^{-1/2}$. For the *k* vs $d^{-1/2}$ plot (square and dashed line), an inverse linear relationship that agrees with the Archard's equation is attained, suggesting continuous improvement in wear performance with decreased grain sizes due to increased HPT-imposed torsional strain levels.

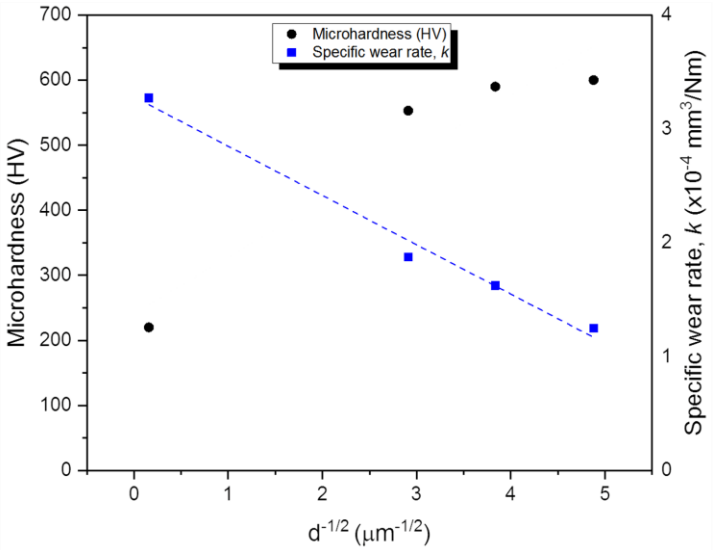

Fig. 10 Microhardness, HV (circle and solid line) and specific wear rate, *k* (square and dashed line) vs inverse square root of grain size.

Interestingly, although the hardness appears to be saturated after 1 HPT revolutions for the HV vs $d^{-1/2}$ plot (circle and solid line), the COF and wear rate, *k* values continue to decrease until 10 HPT revolutions. This implies that the continuous improvement in wear performance is not only a straightforward interrelationship with decreased grain size and increased hardness, but could also be contributed by other factors. Indeed, observation and EDX analysis of the wear features in Figs. 7 and 8, revealed increasing amount of adhered wear particles comprising of largely iron-based oxides with increasing number of HPT revolutions. Such wear features have been found to act as solid lubricants that reduce the frictional force between the test subject and the counter surface that produce smoother wear tracks and lower wear rates. For example, Meng et al. (2019) added CaF_2, hexagonal-BN, WS_2, and graphite particles to enhance the wear resistance of laser surface-textured AISI 316 SS. Alazemi et al. (2017) introduced novel graphene-zinc oxide particles that was able to significantly reduce friction and wear on the surface of steel under high load conditions. Thus, it is reasonable to infer that the higher amounts of these adhered wear particles present on the disk surface after 1 and 10 HPT revolutions are also the main contributors to the improved wear performance, in addition to the decreased grain size and increased hardness.

However, it is worth highlighting that the tribological behaviour of a material is strongly influenced by various factors, including applied load, sliding speed, test period, counter surface material, temperature, and the atmosphere during testing. In fact, some contrasting observations have been made for the tribological behaviour of various SPD-processed metals and alloys, in

which having UFG/NG microstructures and high hardness do not necessarily always translate to improved wear performance, as explained by Gao et al. (2012) in their comprehensive review of the tribological properties of various SPD-processed UFG materials. Nevertheless, it can be concluded that 316L SS typically experience similar wear mechanisms, regardless of the wear rig setup and experimental conditions, which are adhesive, abrasive, tribo-oxidative, or some combination among them, similar to the results obtained in the present study

5. Conclusion

In this study, the L-PBF AM technique of SLM was used to fabricate 316L SS samples. HPT processing was then carried out to induce UFG/NG grain refinement by imposing extreme torsional strains with increased HPT revolutions. After 10 HPT revolutions, strain saturation was achieved, and the mean grain size decreased to ~42 nm compared to ~40 μm before HPT processing.

TEM observations revealed remarkable increase in dislocations as the result of HPT-imposed extreme torsional strains. The microhardness values increased from ~220 HV initially, to ~550 HV after 1/4 HPT revolution. However, only a small increment was observed after 1 revolution (~590 HV), which then saturated at ~600 HV after 10 revolutions.

Dry sliding wear tests demonstrated improved overall wear performance after HPT processing. This was indicated by the reduced COF and *k* values with increased torsional straining from 1/4 up to 10 HPT revolutions. Upon correlation with SEM and EDX analysis, the apparent improvement in wear performance could be attributed to the shallower, smoother, and widely spaced grooves of the wear tracks in the HPT-processed disks compared to the deeper, rougher, and narrow spaced grooves in the as-received counterpart. Furthermore, the wear mechanism transitioned from severe abrasive wear in the as-received disk to a combination of mild abrasive, adhesive, and tribo-oxidative wear after HPT processing. The enhancement in wear performance could be attributed to the higher hardness and UFG and NG microstructures, together with increased amounts of iron oxide-based adhered wear particles that act as solid lubricant to lower the friction between the contact surfaces, both as the result of larger torsional strains imposed upon increased HPT revolutions.

Acknowledgements

S. Mohd Yusuf would like to thank the Faculty of Engineering and Physical Sciences, University of Southampton for his PhD studentship. The TEM experiments were carried out by Y. Chen with financial aids from the National Science Foundation of Fujian Province, China (No. 51601162) and High-Level Talent Funding for Xiamen Oversea Returnee.

Conflict of interest

The authors declare no conflict of interest.

References

Abramova, M.M., Enikeev, N.A., Valiev, R.Z., Etienne, A., Radiguet, B., Ivanisenko, Y., Sauvage, X., 2014. Grain boundary segregation induced strengthening of an ultrafine-grained austenitic stainless steel. Mater. Lett. 136, 349–352. https://doi.org/10.1016/j.matlet.2014.07.188

Alazemi, A.A., Dysart, A.D., Shaffer, S.J., Pol, V.G., Stacke, L.E., Sadeghi, F., 2017. Novel tertiary dry solid lubricant on steel surfaces reduces significant friction and wear under high load conditions. Carbon N. Y. 123, 7–17. https://doi.org/10.1016/j.carbon.2017.07.030

Amanov, A., Lee, S.W., Pyun, Y.S., 2017. Low friction and high strength of 316L stainless steel tubing for biomedical applications. Mater. Sci. Eng. C 71, 176–185. https://doi.org/10.1016/j.msec.2016.10.005

Archard, J.F., 1953. Contact and Rubbing of Flat Surfaces. J. Appl. Phys. 24, 981.

Azushima, A., Kopp, R., Korhonen, A., Yang, D.Y., Micari, F., Lahoti, G.D., Groche, P., Yanagimoto, J., Tsuji, N., Rosochowski, A., Yanagida, A., 2008. Severe plastic deformation (SPD) processes for metals. CIRP Ann. - Manuf. Technol. 57, 716–735. https://doi.org/10.1016/j.cirp.2008.09.005

Bartolomeu, F., Buciumeanu, M., Pinto, E., Alves, N., Carvalho, O., Silva, F.S., Miranda, G., 2017. 316L stainless steel mechanical and tribological behavior — A comparison between selective laser melting , hot pressing and conventional casting. Addit. Manuf. 16, 81–89. https://doi.org/10.1016/j.addma.2017.05.007

Chen, N., Ma, G., Zhu, W., Godfrey, A., Shen, Z., Wu, G., Huang, X., 2019. Enhancement of an additive-manufactured austenitic stainless steel by post-manufacture heat-treatment. Mater. Sci. Eng. A 759, 65–69. https://doi.org/10.1016/j.msea.2019.04.111

Edalati, K., Horita, Z., 2016. A review on high-pressure torsion (HPT) from 1935 to 1988. Mater. Sci. Eng. A 652, 325–352. https://doi.org/10.1016/j.msea.2015.11.074

Gao, N., Wang, C.T., Wood, R.J.K., Langdon, T.G., 2012. Tribological properties of ultrafine-grained materials processed by severe plastic deformation. J. Mater. Sci. 47, 4779–4797. https://doi.org/10.1007/s10853-011-6231-z

Gubicza, J., El-Tahawy, M., Huang, Y., Choi, H., Choe, H., Lábár, J.L., Langdon, T.G., 2016. Microstructure, phase composition and hardness evolution in 316L stainless steel processed by high-pressure torsion. Mater. Sci. Eng. A 657, 215–223. https://doi.org/10.1016/j.msea.2016.01.057

Han, J.K., Lee, H.J., Jang, J. il, Kawasaki, M., Langdon, T.G., 2017. Micro-mechanical and tribological properties of aluminum-magnesium nanocomposites processed by high-pressure torsion. Mater. Sci. Eng. A 684, 318–327. https://doi.org/10.1016/j.msea.2016.12.067

Hokkirigawa, K., Kato, K., 1988. An experimental and theoretical investigation of ploughing , cutting and wedge formation during abrasive wear. Tribol. Int. 51–57.

Hutchings, I.M., 1992. Tribology: Friction and wear of engineering materials, First edit. ed. London.

Karavaeva, M. V., Kiseleva, S.K., Ganeev, A. V., Protasova, E.O., Ganiev, M.M., Simonova, L.A., Valiev, R.Z., 2015. Superior strength of carbon steel with an ultrafine-grained microstructure and its enhanced thermal stability. J. Mater. Sci. 50, 6730–6738. https://doi.org/10.1007/s10853-015-9227-2

Kato, H., 2008. Effects of supply of fine oxide particles onto rubbing steel surfaces on severe – mild wear transition and oxide film formation. Tribol. Int. 41, 735–742.

https://doi.org/10.1016/j.triboint.2008.01.001
Kato, H., Todaka, Y., Umemoto, M., Haga, M., 2015. Sliding wear behavior of sub-microcrystalline pure iron produced by high-pressure torsion straining. Wear 336–337, 58–68. https://doi.org/10.1016/j.wear.2015.04.014
Kato, K., 1997. Abrasive wear of metals. Tribol. Int. 30, 333–338.
Kato, K., 1992. Micro-mechanisms of wear - wear modes. Wear 277–295.
Kawasaki, M., Lee, H.J., Ahn, B., Zhilyaev, A.P., Langdon, T.G., 2014. Evolution of hardness in ultrafine-grained metals processed by high-pressure torsion. J. Mater. Res. Technol. 3, 311–318. https://doi.org/10.1016/j.jmrt.2014.06.002
Kayaba, T., Hokkirigawa, K., Kato, K., 1986. Analysis of the abrasive wear mechanism by successive observations of wear processes in a scanning electron microscope. Wear 110, 419–430.
Lewandowski, J.J., Seifi, M., 2016. Metal Additive Manufacturing: A Review of Mechanical Properties. Annu. Rev. Mater. Res 46, 151–186. https://doi.org/10.1146/annurev-matsci-070115-032024
Li, H., Ramezani, M., Li, M., Ma, C., Wang, J., 2018a. Tribological performance of selective laser melted 316L stainless steel. Tribiology Int. 128, 121–129. https://doi.org/10.1016/j.triboint.2018.07.021
Li, H., Ramezani, M., Li, M., Ma, C., Wang, J., 2018b. Effect of process parameters on tribological performance of 316L stainless steel parts fabricated by selective laser melting. Manuf. Lett. 16, 36–39. https://doi.org/10.1016/j.mfglet.2018.04.003
Meng, R., Deng, J., Duan, R., Liu, Y., Zhang, G., 2019. Modifying tribological performances of AISI 316 stainless steel surfaces by laser surface texturing and various solid lubricants. Opt. Laser Technol. 109, 401–411. https://doi.org/10.1016/j.optlastec.2018.08.020
Mohd Yusuf, S., Chen, Y., Yang, S., Gao, N., 2020. Micromechanical Response of Additively Manufactured 316L Stainless Steel Processed by High-Pressure Torsion. Adv. Eng. Mater. 2000052, 2000052. https://doi.org/10.1002/adem.202000052
Mohd Yusuf, S., Chen, Y., Yang, S., Gao, N., 2019. Microstructural evolution and strengthening of selective laser melted 316L stainless steel processed by high-pressure torsion. Mater. Charact. 159, 110012. https://doi.org/10.1016/j.matchar.2019.110012
Mohd Yusuf, S., Nie, M., Chen, Y., Yang, S., Gao, N., 2018. Microstructure and corrosion performance of 316L stainless steel fabricated by Selective Laser Melting and processed through high-pressure torsion. J. Alloys Compd. 763, 360–375. https://doi.org/10.1016/j.jallcom.2018.05.284
Muley, S.V., Vidvans, A.N., Chaudhari, G.P., Udainiya, S., 2016. An assessment of ultra fine grained 316L stainless steel for implant applications. Acta Biomater. 30, 408–419. https://doi.org/10.1016/j.actbio.2015.10.043
Qin, W., Kang, J., Li, J., Yue, W., Liu, Y., She, D., Mao, Q., Li, Y., 2018. Tribological behavior of the 316L stainless steel with heterogeneous lamella structure. Materials (Basel). 11, 1–12. https://doi.org/10.3390/ma11101839
Rezaei-Nejad, S.S., Abdollah-zadeh, A., Hajian, M., Kargar, F., Seraj, R., 2015. Formation of Nanostructure in AISI 316L Austenitic Stainless Steel by Friction Stir Processing. Procedia Mater. Sci. 11, 397–402. https://doi.org/10.1016/j.mspro.2015.11.008
Roland, T., Retraint, D., Lu, K., Lu, J., 2006. Effect of Surface Nano Crystallization on Tribological Properties of Stainless Steel. Mater. Sci. Forum 524–525, 717–722. https://doi.org/10.4028/www.scientific.net/MSF.524-525.717
Sami, J., Mahdi, C., 2018. The influence of surface nanocrystallization on structural, tribological and electrochemical properties of 316 L. AIP Conf. Proc. 1976, 1–5. https://doi.org/10.1063/1.5042374
Scheriau, S., Zhang, Z., Kleber, S., Pippan, R., 2011. Deformation mechanisms of a modified 316L austenitic steel subjected to high pressure torsion. Mater. Sci. Eng. A 528, 2776–2786. https://doi.org/10.1016/j.msea.2010.12.023
Sun, Y., Moroz, A., Alrbaey, K., 2014. Sliding wear characteristics and corrosion behaviour of selective laser melted 316L stainless steel. J. Mater. Eng. Perform. 23, 518–526. https://doi.org/10.1007/s11665-013-0784-8
Thorvaldsen, A., 1997. The intercept method—1. Evaluation of grain shape. Acta Mater. 45, 587–594. https://doi.org/10.1016/S1359-6454(96)00197-8
Triwiyanto, A., Hussain, P., Rahman, A., Ismail, M.C., 2013. The Influence of Nitriding Time of AISI 316L Stainless Steel on Microstructure and Tribological Properties. Asian J. Sci. Res. 6, 323–330.
Valentini, L., Schino, A. Di, Kenny, J.M., Gerbig, Y., Haefke, H., 2002. Influence of grain size and film composition on wear resistance of ultra fine grained AISI 304 stainless steel coated with amorphous carbon films. Wear 253, 458–464.
Wang, C.T., Gao, N., Wood, R.J.K., Langdon, T.G., 2011. Wear behavior of an aluminum alloy processed by equal-channel angular pressing. J. Mater. Sci. 46, 123–130. https://doi.org/10.1007/s10853-010-4862-0
Wongsa-Ngam, J., Kawasaki, M., Langdon, T.G., 2013. A comparison of microstructures and mechanical

properties in a Cu-Zr alloy processed using different SPD techniques. J. Mater. Sci. 48, 4653–4660. https://doi.org/10.1007/s10853-012-7072-0
Yusuf, S.M., Gao, N., 2017. Influence of energy density on metallurgy and properties in metal additive manufacturing. Mater. Sci. Technol. (United Kingdom) 33. https://doi.org/10.1080/02670836.2017.1289444
Zhilyaev, A.P., Nurislamova, G. V., Kim, B.K., Bar??, M.D., Szpunar, J.A., Langdon, T.G., Baró, M.D., Szpunar, J.A., Langdon, T.G., 2003. Experimental parameters influencing grain refinement and microstructural evolution during high-pressure torsion. Acta Mater. 51, 753–765. https://doi.org/10.1016/S1359-6454(02)00466-4
Zhu, Y., Zou, J., Chen, X., Yang, H., 2016. Tribology of selective laser melting processed parts: Stainless steel 316 L under lubricated conditions. Wear 350–351, 46–55. https://doi.org/10.1016/j.wear.2016.01.004